Pre-straining effect on ferrite/pearlite anisotropic transformation strain in steels by

Takayuki Otsuka, Renald Brenner, Brigitte Bacroix

Pre-straining effect on ferrite/pearlite anisotropic transformation strain in steels

by

Takayuki OTSUKA
Corresponding author
Research & Development, Nippon Steel Corporation, 20-1 Shintomi Futtsu Chiba 293-8511 Japan
otsuka.6gx.takayuki@jp.nipponsteel.com

Renald BRENNER
Institute Jean Le Rond d'Alembert, Sorbonne Université, 4 Place Jussieu, 75252 Paris Cedex 05 France

Brigitte BACROIX
Laboratoire des Sciences des Procédés et des Matériaux, Université Sorbonne Paris Nord, 99 Av Jean-Baptiste Clément 93430 Villetaneuse France

Abstract

The effect of pre-straining on ferrite/pearlite phase transformation in high strength steels is investigated. Two steels differing mainly in their Nb content (0.03C 0.68Si 1.82Mn 0.00 or 0.04Nb in mass%) are either pre-tensioned or pre-compressed and the same-directional transformation strain is measured. A crystal plasticity fast Fourier transform numerical model with back stress effect is used for further investigation and the results are compared. Experimentally, it was found that 30% pre-tension reduces the transformation strain in the same direction by 0.09% (0.00Nb) and 0.13% (0.04Nb), while 30% pre-compression increases it by 0.16% (0.00Nb) and 0.02% (0.04Nb). The numerical simulation estimates the experimentally observed anisotropic transformation strain. In the numerical simulation, even though the anisotropy in transformation plasticity has been qualitatively reproduced, a larger anisotropy effect was observed. The quantitative discrepancies found in between experimental results and numerical results are due to the annihilation of dislocations during the interval between the pre-straining and the onset of phase transformation. The anisotropy in transformation strain found in the experiments is large enough to cause an unacceptable dimensional change in e.g. heat treated steel sheet products.

Key words; Transformation plasticity, High strength steel, Pre-deformation, Back stress, Crystal plasticity, FFT

1. Introduction

Production of steel sheets requires a succession of forming and heat treatment steps that must be rigorously controlled to optimise the final properties of the sheets. In the case of steels, heat treatment often involves phase transformation and this phenomenon is of primary importance in terms of the quality of the final products; it is also in most cases coupled with a deformation step to achieve the desired shape and accurate dimensions. For example, in a hot strip steel rolling mill, the final tandem rolling of the hot strip is followed by a cooling process in a run-out table (ROT) where phase transformation takes place. Another example is the hot stamping process in which the forming step is followed by quenching to produce a high-strength martensitic structure and final tempering to reduce the phase transformation induced residual stresses.

For the development of thermo-mechanical simulations aiming at predicting final residual stresses and distortion in such cases, it is essential to characterise and understand the phase transformation phenomena occurring after a pre-deformation step, during e.g. a cooling step.

The pioneering research in this field has been made by Taleb and Petit [1-2]. A 16MND5 (French standard) steel containing 0.17C 0.25Si 1.44Mn (mass%) has been considered in their research and these authors have investigated the effect of a pre-deformation by tension/compression/torsion on

subsequent martensite [1] and bainite [2] transformation plasticity. The results show an opposite effect of the pre-deformation on the transformation plasticity; namely, the transformation strain develops in a direction opposite to the pre-deformation direction for the bainitic transformation, whereas the same direction is observed for the martensitic transformation. In the case of the bainitic transformation, it has also been reported that the back stress, induced during the pre-deformation process, has a direct influence on the residual stresses and shape/dimensions of the hot rolled strip final products. A back-stress description has therefore been considered in their model in a satisfactory way to reproduce the experimental results. These experiments have been conducted at relatively low phase transformation temperatures though (i.e. ranging from 380 to 580 °C), as they considered only bainite and martensite phase transformations. However, in the case of hot steel strip rolling, hot rolling is conducted at much higher temperatures, i.e. within the austenitic range, and, subsequently, in most cases, transformation to ferrite/pearlite occurs. Again, the final dimensions and shape of the strip may vary depending on the actual amount and direction of the transformation strain, which depends in turn of the hot-rolling step. Thus, it is also of primary importance to investigate the influence of an initial pre-deformation at high temperature on subsequent transformation kinetics, to be able to better control the final mechanical and geometrical characteristics of hot rolled products.

This question is not new and has already been addressed for many different steel grades, as well as for various pre-deformation modes and cooling rates inducing different phase transformations. For example, in a recent study, Oshita et al. [3] used a 3-point bending system to identify the transformation plasticity under externally applied stress in an S45C (Japanese standard) steel containing 0.45C (mass%), after pre-strain at high temperature. In such a case, it was shown that the transformation plastic strain decreases with increasing pre-plastic deformation (performed in tension within the austenitic range). However, neither the stress-free condition nor the influence of the pre-strain direction was investigated in this case. Li et al. [4] also investigated the influence of a pre-strain on transformation in a high carbon chromium steel pre-deformed in tension at 900 °C whereas Schicchi et al. [5] treated the case of a 22MnB5 steel deformed also in tension at 950 °C. In both cases, it was shown that such a pre-strain at high temperature had a strong influence on the incubation time for transformation, but not on the actual transformation process. This was justified by the presence of defects within the austenitic matrix due to deformation (dislocation structures) acting as nucleation sites for bainite and enhancing the C diffusion. Drillet et al. [6-7] also showed an early onset of phase transformation in the case of a more complex deformation mode (hot stamping) imposed on Usibor steel grades (22MnB5 AlSi, an aluminised boron steel). They concluded that the effect is caused by the sites created by the initial plastic deformation at high temperature which favour in turn ferrite nucleation at the austenite grain boundaries. They also indicate that the temperature at which the initial plastic deformation is applied plays an important role in this modification [6]. Some other studies (e.g. [4, 8-12]) try to explain the final shape after deformation and cooling only by the characteristics of the

cooling step, without considering at all the influence of the pre-strain.

Thus, most previous studies report a change in the onset of phase transformation (an increase of the temperature) due to initial plastic deformation of austenite (see also [7]) but do not give further details on how this phase transformation kinetics is modified by pre-strain. Therefore, there is still a need for an investigation of the pre-deformation effect on transformation strain at elevated temperatures inducing ferrite or pearlite phase transformations in order to better understand this particular phenomenon. The present work brings new results on this question by providing both numerical modelling and experimental aspects (as detailed further in this paper) showing how and why the transformation strain itself is affected by the pre-strain.

One aim of this work is specially to investigate the directional effect of a pre-deformation on the transformation strain in ferrite/pearlite phase transformations in steels. In order to do so, simple tension and compression tests were conducted at high temperatures before a cooling step, allowing phase transformation. Although these deformation modes differ from the industrial hot rolling process, they allow a precise measurement of the transformation strains after deformation. Also, in contrast to the martensitic phase transformation, which strongly depends on the deformation mode and strain path especially under applied stress [14-16], the ferrite/pearlite phase transformation is not a shear type but a diffusional transformation. Therefore, it is thought to be slightly less sensitive to the actual deformation mode, especially under stress-free phase transformation conditions.

In order to interpret the obtained experimental results, a micromechanical numerical model [17-18] taking into account the back stress effect has been developed [8] in the framework of crystal plasticity considering back-stress effect [20-23]. Again here, it must be said that numerous previous works report numerical simulations of phase transformation in steels, based on crystal plasticity. But most of them deal only with the martensitic transformation under applied stress (i.e. combined with plastic deformation) and perform finite element simulations, which most often involve a simplified description of the initial microstructures of the materials (initial texture and deformation state) in order to reduce the computing time.

For example, Park et al. [9] have developed an advanced constitutive modelling (included into an FE code) and calibration methodology (using in-situ high energy X-ray diffraction to get mechanical and microstructural data) based on rate-independent crystal plasticity to predict the quasi-static macroscopic behaviour of 3rd generation multiphase advanced high strength steels (3GAHSS) prepared with a quenching and partitioning (Q&P) process. Although their efforts are quite impressive, they treat exclusively the question of the interaction between plasticity and transformation at room temperature, neglecting all thermal effects, and thus do not capture the temperature dependence of transformation. More recently, Connolly et al. [10] have developed a new thermodynamically consistent rate-dependent crystal plasticity model to simulate the large deformation behaviour of Q&P steels with TRIP effect. The proposed model is claimed to be one of the first constitutive models, if

not the first, suitable for a wide range of strain-rates and temperatures. This model also includes coupling between plastic slip and transformation, and which explicitly takes into account a detailed description of the initial state. These striking attempts have successfully simulated the TRIP behaviours of steels, based on displacive mechanisms.

In the present case, as the ferrite/pearlite phase transformation is considered to be a diffusive mechanism, it is assumed to be more dependent on time than on dislocation mechanisms. Thus, a time-dependent iso-thermal phase transformation mechanism is introduced in the framework of crystal plasticity in order to calculate the transformation strain obtained during a thermal treatment step [17, 26-29], following a pre-deformation [19, 30]. A back-stress induced by this deformation is taken into account in the model to describe the influence of the pre-deformation and the Fast Fourier Transformation (FFT) – based formulation is used to significantly decrease the computation time and efficiency compared to FE simulations [31-33]. The calculated strains are then compared to the experimental ones, in order to check the capacity of the proposed modelling approach to satisfactorily reproduce the diffusive transformation behaviour after a pre-deformation at high temperature and to account for the directional effect of the pre-strain.

2. Experimental approach

This section describes the experimental procedures for the measurement of the anisotropic transformation strain and experimental results are then detailed.

2.1. Experimental devices

In the present work, the pre-deformation step is carried out by tension and compression tests, both up to 30% in engineering strain, which is close to what is imposed to the steel on the hot rolling mills. To achieve this, two different equipment are used; one is an Instron 8803 type fatigue machine equipped with atmosphere and temperature control for pre-tension testing, and the other is a Bähr compression machine for pre-compression testing. The reason why we used the different machine for the tests with compression is to avoid a buckling. Potentially, the 2-dimensional Digital Image Correlation (DIC) method can be used to measure the in-plane strain with novel methods for the correction of the effect of out-of-plane displacement [34-35], or 3-dimentional DIC [11] can also applied. The DIC method can be applied to a high temperature measurement up to 1200 ^{o}C [12]. However, considering the length between two grips of the fatigue machine, a significant out-of-plane displacement can be occurred. In this case, a simple compressive machine is useful for the large compressive strain application.

1

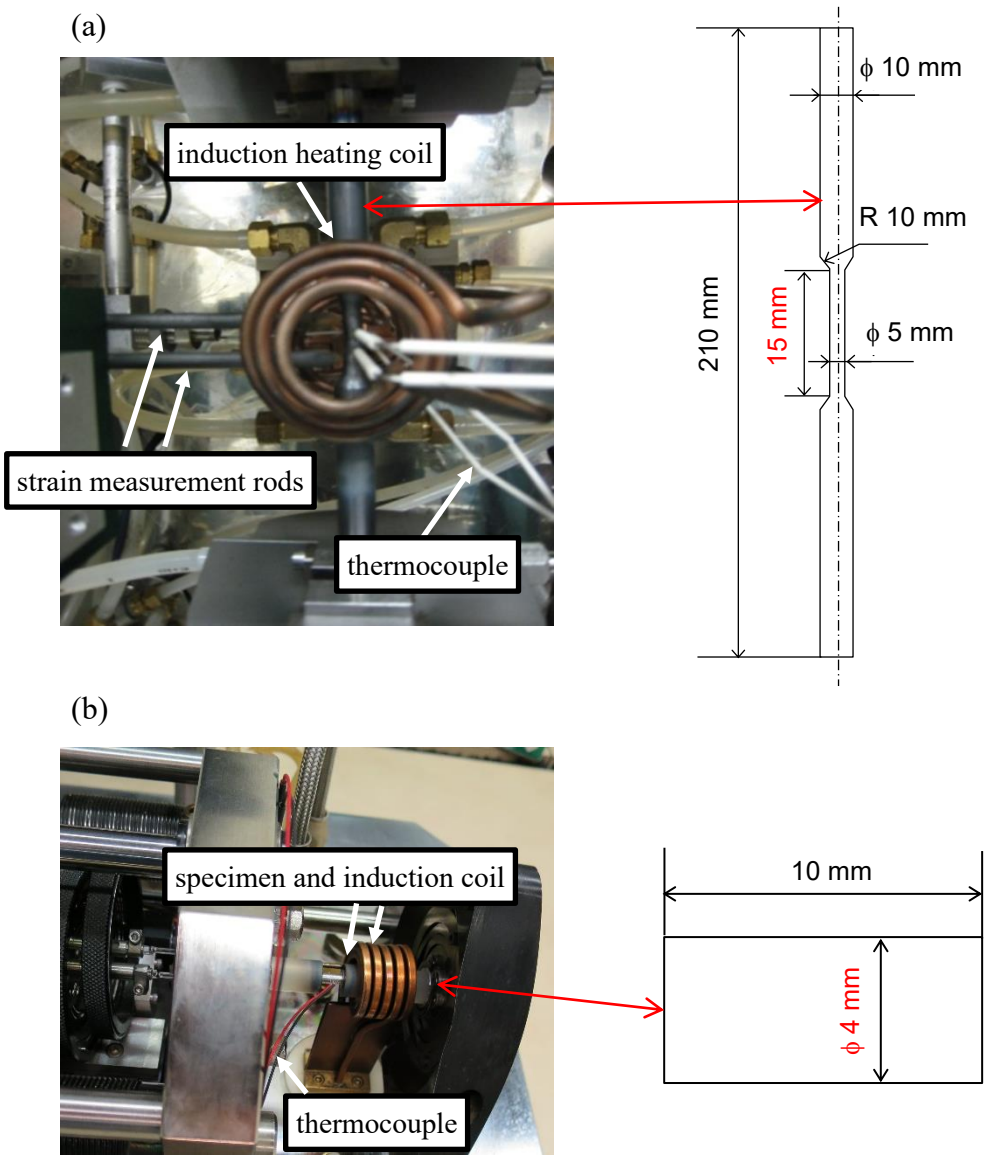

Fig. 1 The specimen setup of the tensile testing machine (a) and its specimen geometry for the pre-tension tests. The machine is equipped with the high temperature extensometer for strain measurement and the induction heating system for temperature control. For this machine, only the temperature of the central part of the specimen (12.5 mm gauge length) is controlled and the strain is measured.

For the compressive test, the compression machine uses the specimen geometry shown in (b). This device is also equipped an induction heating system for temperature control. The induction coil is designed to achieve uniform temperature.

2

3 The experimental setup for the pre-tension test is shown in Fig. 1, the interior of the vacuum chamber
4 (a). The induction coil allows a sample to be heated while the nozzle injects helium gas into the gauge

length zone (= 12.5 mm) to cool it. Strain is measured during the tests using a high temperature extensometer which measures the distance of the gauge through the ceramic rods which are in direct contact with the specimen. The Bähr apparatus used for the pre-compression tests is shown in Fig. 1 (b) with the geometry of the specimens used for the pre-compression tests.

The samples were prepared by vacuum casting, hot rolling and tempering. A 50 mm thick slab was cast in the vacuum chamber, then hot rolled into a 20 mm thick strip and annealed at 800 °C for 3 hours. The specimens were mechanically machined and ground, and thus the specimen's diameter does not correspond to the hot rolled slab thickness.

2.2. Experimental conditions

The chemical compositions of the two 590 MPa tensile strength steel grades used in this study, designated HSS1 and HSS2, are shown in Table 1. Steel grade HSS1 has no Nb content and its Ar_3 and Ar_1 points are 729 °C and 663 °C respectively, while HSS2 contents 0.04 mass% Nb and its Ar_3 and Ar_1 points are 680 °C and 596 °C respectively. Nb precipitates are known to hinder recovery, recrystallisation and phase transformation and thus, Nb is sometimes added to better control the final microstructure of the hot steel rolling products [13]. So, in order to also determine the effect of the Nb content on the transformation strain after pre-deformation, two steel grades with different Nb content are selected. The imposed temperature and stress sequences are summarised in Fig. 2. The specimen is heated up to 950 °C and held for 5 min to achieve full austenitisation and homogenisation. Note that at this temperature the Nb content is not considered to be in full solution and therefore the effect of Nb may be less significant than expected, given the weight percentage contained in the HSS2 grade. The specimen is then cooled at the controlled cooling rate of 5 K/s, which allows to obtain a ferrite/pearlite phase at ambient temperature, as explained below.

Fig. 3 shows the microstructure etched by 3% Nital solution to reveal ferrite/pearlite grain boundaries and observed at ambient temperature in optical microscopy after heat treatment of HSS1 (a) and HSS2 (b). The mean ferrite grain size is 59.7 μm for HSS1 and 48.1 μm for HSS2 respectively. The smaller grain size in HSS2 reflects the effect of Nb content. During the cooling sequence, an instantaneous tensile/compressive stress above the yield stress is applied to the specimen just prior the onset of phase transformation (A_{r3} point) at 750 °C for HSS1 and 720 °C for HSS2, which results in the target plastic strain (-30, 0, 10, 20, 30%). The time interval from when the stress reaches zero due to unloading to when the temperature reaches Ar_3 point was 3 s for HSS1 and was 12 s for HSS2. The strain variation is then continuously measured during cooling. In order to study the effect of pre-straining on transformation strain, a shorter period between pre-straining and phase transformation is preferred to avoid the possible annihilation of dislocations by a creep mechanism at relatively high temperature.

Therefore, taking into account the response time, the interval between pre-tension (compression), unloading and the onset of phase transformation is determined for each testing machine.

Table 1 Chemical compositions of HSS1 and HSS2 (mass%). The difference between these two steel grades is in their Nb content to evaluate the precipitation effect.

	C	Si	Mn	P	S	Nb	Al
HSS1	0.03	0.68	1.82	0.006	0.002	0.00	0.01
HSS2	0.03	0.68	1.82	0.006	0.002	0.04	0.01

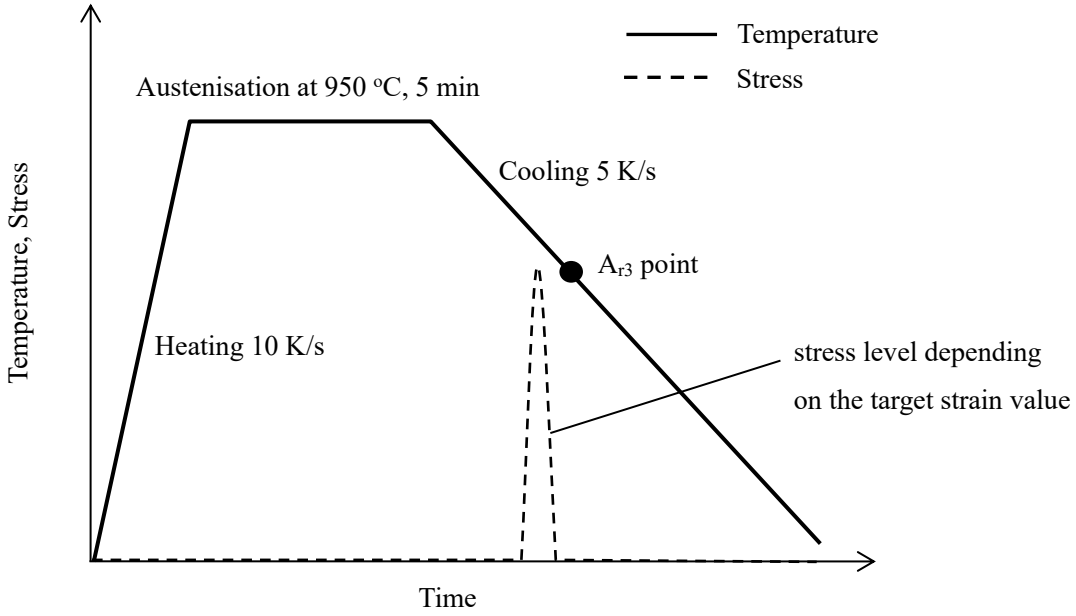

Fig. 2 Imposed temperature and stress sequence. Full austenisation is made at 950 °C for 5 min holding, which is followed by controlled cooling at the rate of 5 K/s. Both tensile and compressive stresses are applied right before the onset of phase transformation. Right after the strain reaches the target value, unloading is processed to measure the transformation strain under stress free condition.

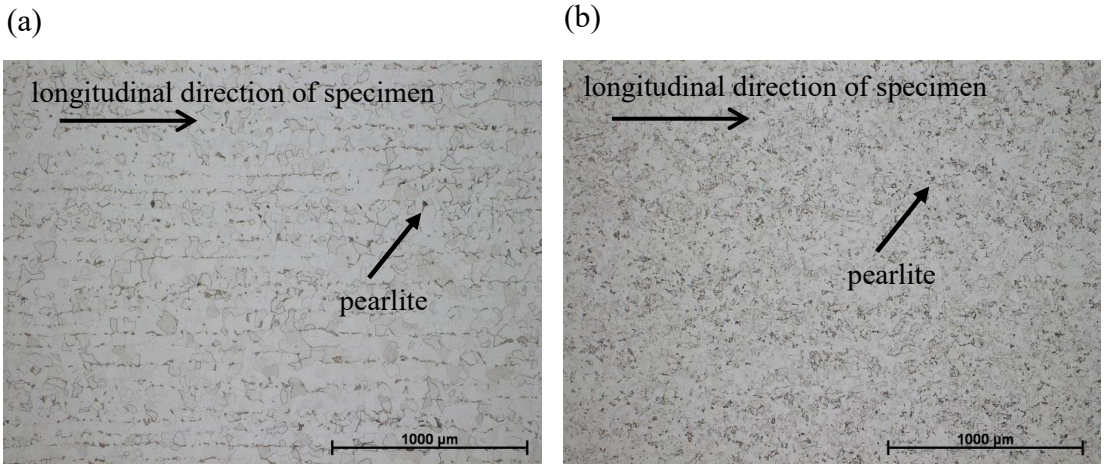

Fig. 3 Microstructures obtained by optical microscopy after heat treatment (without pre-straining) of HSS1 (a) and HSS2 (b). Both HSS1 and HSS2 have ferrite and pearlite mixed phase. The mean grain size is 59.7 µm for HSS1 and 48.1 µm for HSS2 respectively.

2.3. Experimental results and discussion

The obtained strain curves contain the contributions of the mechanically induced plastic strain, the thermal strain and the transformation strain. In order to extract the sole transformation strain, the following procedure is applied. The A_{r3} point has first been estimated by preliminary dilatometry tests, and then the deformation is applied just above this pre-determined temperature. As this pre-deformation (followed by stress release) induces plastic strain, this residual plastic strain is eliminated from the total strain. Next, by assuming that the thermal strain varies linearly with temperature, one can eliminate the thermal strain from the total strain to obtain the sole transformation strain as follows. As the coefficients of linear thermal expansion of the austenite and the ferrite/pearlite phases are different, two approximation lines can be drawn on a strain versus temperature plot for austenite and ferrite/pearlite and the volume fraction of each phase can be calculated using the Lever rule. This procedure is schematically explained in Fig. 4.

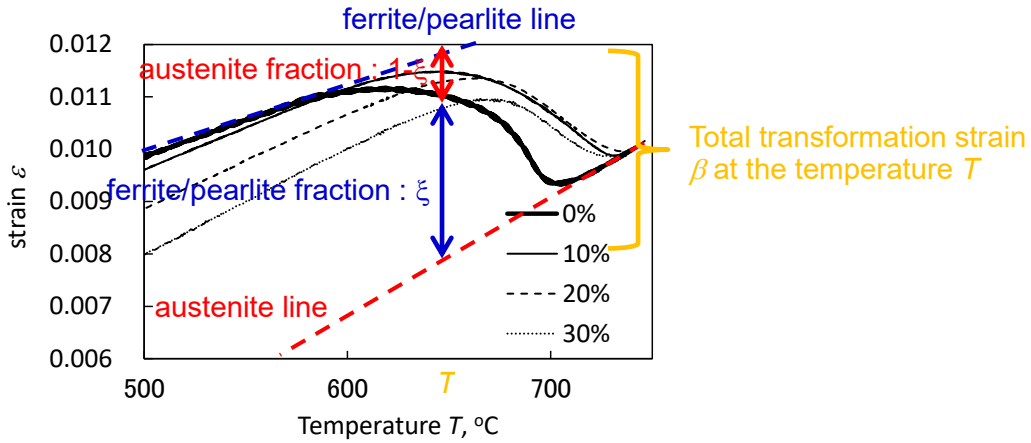

Fig. 4 Transformed fraction estimation procedure.

With this estimation of the volume fraction and thermal strain, the transformation strain in HSS1 steel grade is extracted from the data and presented in Fig. 5 (a) for pre-tension, and (b) for pre-compression respectively. Note that the case without pre-strain has also been treated on both machines and thus 0% strain curves are determined for both pre-tension and pre-compression. We assume the discrepancy found in 0% initial strain cases measured by both machines was caused by the temperature distribution in the radial direction in the specimen.

From Fig. 5 (a) and (b), it can be seen that the transformation onset temperature is increased for both the pre-tension case and pre-compression cases. As mentioned in the introduction part, this is believed to be due to the dislocations induced during pre-straining acting as new phase nuclei and accelerating the phase transformation. It is also clear that the magnitude of the transformation strain in the measured direction, i.e. the pre-strain direction, decreases with the value of the pre-tension strain, and increases with the value of the pre-compression strain. Fig. 5 (c) summarises the dependence of the initial strain on the extracted transformation strain values for the HSS1 steel grade. The standard deviation for the case of 0% initial strain with the tensile machine is 5.7×10^{-5}, which means the data are quite reliable.

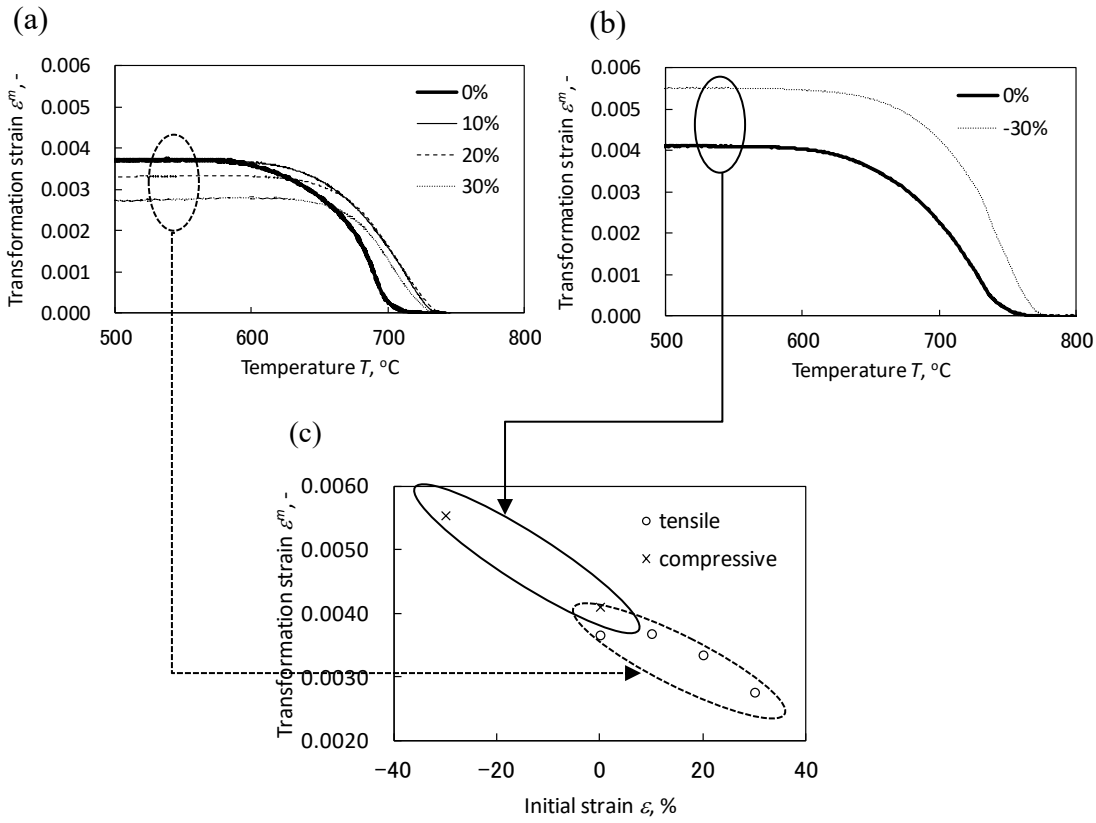

Evolution of the transformation strain with temperature and pre-strain for the HSS1 steel. The measured transformation strain decreases with pre-tension (a), while it increases with pre-compression (b).

Fig. 5

The obtained transformation strain values are presented in (c) as a function of initial strain (pre-strain) value.

The same procedure is applied to HSS2 steel grade and the results are shown in Fig. 6 (a) for pre-tension and (b) for pre-compression. The overall tendency is found to be similar to that of HSS1, although the influence of the pre-strain level appears to be marginal (especially for pre-compression). This may be attributed to the flow curve difference between the two steel grades. As discussed in section 3.3, strain hardening is more significant in HSS1 than in HSS2 and this leads to a greater accumulation of dislocations with the development of back stress. The summarised relation between initial strain and transformation strain in HSS2 is shown in Fig. 6 (c), where it is seen again that the transformation strain in the pre-straining direction decreases with pre-tension and increases with pre-compression.

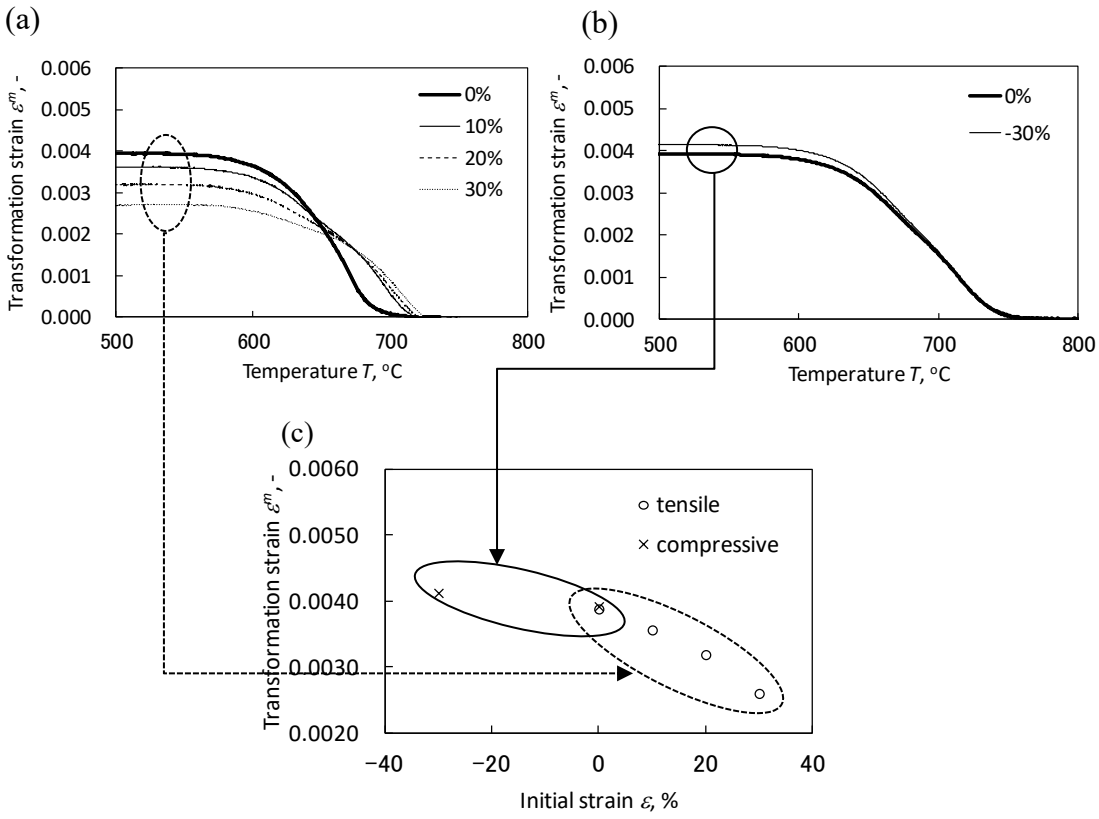

Fig. 6 Evolution of the transformation strain with temperature and pre-strain for the HSS2 steel. The measured transformation strain decreases with pre-tension (a), while it increases with pre-compression (b).
The obtained transformation strain values are presented in (c) as a function of initial strain (pre-strain) value.

3. Numerical simulation of the effect of pre-straining on transformation strain

The aim of this section is to model the effect of pre-straining on the transformation strain using a micromechanical approach. For this purpose, a fast Fourier transform (FFT)-based [14] micromechanical crystal plasticity model [40-43] is used. The authors have previously extended the model to diffusive phase transformation problems and successfully reproduced the transformation plasticity phenomena for a carbon steel [15]. This model is further extended in the present study by considering the Armstrong-Frederick (A-F) type back-stress model [16], which can be easily included into the crystal plastic formalism [44-46] or modified A-F model [47-48]. Note that the aim of this section is not to find the fitting parameters that appear in the model but to describe properly the mechanical behaviour under cooling after pre-strain and to propose some mechanisms responsible for the anisotropy of the transformation strain. The details of the constitutive models and governing equations are presented below.

3.1. FFT-based formulation

For a heterogeneous elasto-plastic material, the rate-form of the constitutive relation at a local position x reads:

$$\dot{\boldsymbol{\sigma}}(\boldsymbol{x}) = \boldsymbol{C}(\boldsymbol{x}): \dot{\boldsymbol{\varepsilon}}^{e}(\boldsymbol{x}) = \boldsymbol{C}(\boldsymbol{x}): (\dot{\boldsymbol{\varepsilon}}(\boldsymbol{x}) - \dot{\boldsymbol{\varepsilon}}^{p}(\boldsymbol{x}) - \dot{\boldsymbol{\varepsilon}}^{m}(\boldsymbol{x})) \tag{1}$$

where $\boldsymbol{C}(x)$ is the elastic tensor and $\boldsymbol{\varepsilon}^{e}$, $\boldsymbol{\varepsilon}$, $\boldsymbol{\varepsilon}^{p}$ and $\boldsymbol{\varepsilon}^{m}$ are the elastic, total, plastic and transformation strain tensors respectively. Note that the local transformation strain $\boldsymbol{\varepsilon}^{m}$ is isotropic and that the thermal strain is not considered in the present calculations. Although the transformation develops as the temperature decreases, the temperature can be considered to be uniform in the RVE described by 100 austenite grains. This means that the thermal strain does not contribute to the stress development and thus it can be neglected. By introducing a homogeneous reference media with elasticity $\boldsymbol{C}^{0}$, equation (1) can be rewritten as:

$$\begin{gathered} \dot{\boldsymbol{\sigma}}(\boldsymbol{x}) = \boldsymbol{C}^{0}: \dot{\boldsymbol{\varepsilon}}(\boldsymbol{x}) + (\boldsymbol{C}(\boldsymbol{x}) - \boldsymbol{C}^{0}): \dot{\boldsymbol{\varepsilon}}(\boldsymbol{x}) - \boldsymbol{C}(\boldsymbol{x}): (\dot{\boldsymbol{\varepsilon}}^{p}(\boldsymbol{x}) + \dot{\boldsymbol{\varepsilon}}^{m}(\boldsymbol{x})) = \boldsymbol{C}^{0}: \dot{\boldsymbol{\varepsilon}}(\boldsymbol{x}) + \dot{\boldsymbol{\tau}}(\boldsymbol{x}) \\ \forall x \in V, \quad \mathrm{div}\dot{\boldsymbol{\sigma}} = 0 \quad \forall x \in V, \quad \dot{u}^{'} \#, \quad \dot{\boldsymbol{\sigma}} \cdot \boldsymbol{n} - \# \end{gathered} \tag{2}$$

where $\dot{\boldsymbol{\tau}}(\boldsymbol{x})$ is a polarisation tensor and the abbreviation form $\#$ represents the periodic boundary condition. Equation (2) is rewritten in a Fourier space as:

$$\hat{\boldsymbol{\sigma}}(\boldsymbol{\xi}) = \mathrm{i}\boldsymbol{C}^{0}: \left(\widehat{\boldsymbol{u}}^{'}(\boldsymbol{\xi}) \otimes \boldsymbol{\xi}\right) + \hat{\boldsymbol{\tau}}(\boldsymbol{\xi}), \qquad \mathrm{i}\hat{\boldsymbol{\sigma}}(\boldsymbol{\xi}) \cdot \boldsymbol{\xi} = 0 \tag{3}$$

where, $\boldsymbol{\xi}$ is frequency, and the non-italic character i represents imaginary number. By eliminating $\widehat{\boldsymbol{\sigma}}$ from equation (3), we obtain

$$\widehat{\boldsymbol{u}}^{'}(\boldsymbol{\xi}) = \frac{\mathrm{i}}{2}(\boldsymbol{N}^{0} \otimes \boldsymbol{\xi} + \boldsymbol{\xi} \otimes \boldsymbol{N}^{0})\hat{\boldsymbol{\tau}}(\boldsymbol{\xi}) \tag{4}$$

where

$$\boldsymbol{N}^{0}(\boldsymbol{\xi}) = \boldsymbol{K}^{0}(\boldsymbol{\xi})^{-1}, \ \boldsymbol{K}^{0}(\boldsymbol{\xi}) = \boldsymbol{C}^{0}: (\boldsymbol{\xi} \otimes \boldsymbol{\xi}) \tag{5}$$

$$\hat{\boldsymbol{\varepsilon}}(\boldsymbol{\xi}) = \frac{\mathrm{i}}{2}\left(\boldsymbol{\xi} \otimes \widehat{\boldsymbol{u}}^{'}(\boldsymbol{\xi}) + \widehat{\boldsymbol{u}}^{'}(\boldsymbol{\xi}) \otimes \boldsymbol{\xi}\right) = -\widehat{\boldsymbol{\Gamma}}^{0}(\boldsymbol{\xi}): \hat{\boldsymbol{\tau}}(\boldsymbol{\xi}) \tag{6}$$

$$\widehat{\boldsymbol{\Gamma}}^{0}(\boldsymbol{\xi}) = \frac{1}{4}\left(N^{0}_{li}\xi_j\xi_k + N^{0}_{ki}\xi_j\xi_l + N^{0}_{lj}\xi_i\xi_k + N^{0}_{kj}\xi_i\xi_l\right) \tag{7}$$

$\widehat{\boldsymbol{\Gamma}}^{0}$ is a periodic Green's operator. Inverse Fourier transformation of equation (6) gives the strain field within the heterogeneous medium. The details of the solution are given in references [17, 39].

3.2. Constitutive equations for crystal plasticity with back stress effect

In this research, the conventional single crystal constitutive equations are applied [49-51]. The total plastic strain rate can be obtained as a sum of the individual slip rate $\dot{\gamma}^{\alpha}$ on the α slip system. Introducing a Schmid tensor $\boldsymbol{p}^{\alpha}$ for slip system α, the total plastic strain rate can be written as:

$$\dot{\boldsymbol{\varepsilon}}^p = \sum_\alpha \boldsymbol{p}^\alpha \dot{\gamma}^\alpha \tag{8}$$

where $\boldsymbol{p}^\alpha$ is defined as:

$$\boldsymbol{p}^\alpha = \frac{1}{2}(\boldsymbol{s}^\alpha \otimes \boldsymbol{m}^\alpha + \boldsymbol{m}^\alpha \otimes \boldsymbol{s}^\alpha), \tag{9}$$

$\boldsymbol{s}^\alpha$ and $\boldsymbol{m}^\alpha$ are respectively the slip direction and slip plane normal of the α slip system. When the effective resolved shear stress $\tau^{*(\alpha)}$ becomes equal to the Critical Resolved Shear Stress (CRSS) g^α, the slip system α becomes active, such that:

$$\left|\tau^{*(\alpha)}\right| = |\boldsymbol{p}^\alpha : \boldsymbol{\sigma}| = g^\alpha \tag{10}$$

with the effective resolved shear stress

$$\tau^{*(\alpha)} = \tau^{(\alpha)} - a^{(\alpha)}. \tag{11}$$

The back stress $a^{(\alpha)}$ on the α slip system is modelled as follows using the Armstrong-Frederick (A-F) model [16]:

$$\dot{a}^{(\alpha)} = C\dot{\gamma}^{(\alpha)} - d a^{(\alpha)}\left|\dot{\gamma}^{(\alpha)}\right|. \tag{12}$$

In this research the rate-independent model proposed by Hutchinson [17] is also used. In this case, the hardening law is expressed by:

$$\dot{\boldsymbol{\sigma}} : \boldsymbol{p}^\alpha = \sum_\beta h^{\alpha\beta}\dot{\gamma}^\beta \tag{13}$$

which implies:

$$\dot{g}^\alpha = \sum_\beta h^{\alpha\beta}\left|\dot{\gamma}^\beta\right| \tag{14}$$

where $h^{\alpha\beta}$ are the so-called hardening coefficients. For the description of these coefficients, the following model is used [18]:

$$h^{\alpha\alpha} = h = H_0 \operatorname{sech}^2\left[\frac{H_0 \sum_\beta \left|\gamma^\beta\right|}{\tau_s - \tau_0}\right] \tag{15}$$

$$h^{\alpha\beta} = qh + (1-q)h\delta_{\alpha\beta} \tag{16}$$

where H_0 is the coefficient parameter, τ_0 is the initial yield stress value and τ_s is the saturated stress value and q is the latent hardening parameter.

3.3. Calculation conditions

$64 \times 64 \times 64$ calculation points are uniformly defined within a cubic RVE. The boundary conditions for displacement, strain and stress are $x - y - z$ periodic. Inside the RVE, 100 initial grains with random orientation are created, using the Voronoi tessellation technique.

First of all, the mechanical parameters listed in Table 2 are determined by fitting the measured stress-strain curves (s-s curves) determined just before and after phase transformation, i.e. for the austenite and ferrite/pearlite phases respectively. Note that only one slip system family, namely the {111}<110>

(12 slip systems) is considered for the austenitic phase, whereas three slip system families are considered for the ferrite/pearlite phase, namely the {110}<111>, {112}<111> and {123}<111> slip system families (48 slip systems). For the sake of simplicity, these 3 slip system families are assumed to have the same parameters listed in Table 2. Here, the latent hardening parameter q is a function of steel grade and temperature. Ideally, this parameter should be also identified together with the other hardening parameters. However, the mechanical behaviour during phase transformation can be reproduced by optimising other parameters appearing in Table 2 and, furthermore, the identification process of the value at high temperature is extremely difficult and unrealistic. Therefore, in this study, the value of 1.0 is used for all the simulation cases [19]. Initially, the s-s curves of both the austenite and ferrite/pearlite phases were measured at a temperature of 750 ^{o}C for HSS1 and 720 ^{o}C for HSS2, which is just above the A_{r3} point of each steel grade. For the austenite phase, the s-s curves are measured immediately after reaching the pre-set temperature and the temperature is controlled to be constant during the straining. For the ferrite/pearlite phase, the temperature is controlled to be constant after reaching the fixed temperature until the phase transformation is completed. The transformation completion time is estimated from the preliminary obtained TTT curve. The s-s curves of the ferrite/pearlite phase are measured after this isothermal hold. Note that in real industrial phenomena, the temperature decreases with time. However, it is difficult to identify the temperature dependent s-s curves of each pure phase, so for simplicity the s-s curves at fixed temperatures are used in this research. Fig. 7 compares the calculated stress-strain curves using manually fitted parameters on the measured ones for austenite (a) and ferrite/pearlite (b) in HSS1 and austenite (c) and ferrite/pearlite (d) in HSS2. For both steel grades, the austenite phase has a slightly lower yield stress but higher flow stress at relatively high strain range, implying a larger work hardening capacity. This tendency agrees with the work hardening behaviours of the austenitic and ferritic stainless steel [55-56]. Concerning the yield stress difference in ferrite/pearlite phase between HSS1 and HSS2, the yield stress (0.2% proof stress) in HSS1 is 63.2 MPa while in HSS2 is 113.2 MPa. This discrepancy in two different steel grades may be due to grain size effect and/or Nb(C, N) precipitation effect [20]. Considering the measured mean grain size (HSS1:59.7 μm and HSS2:48.1 μm) and Hall-Petch relation in steels [58-60], the effect of grain size on the yield stress may be less significant. Although some discrepancy can be observed in the austenite phase of HSS1 above 0.05 strain, the higher priority was given to strains below 0.05 reflecting the magnitude of the ferrite/pearlite transformation strains. The parameter set shown in Table 2 is not the unique solution of a good fitting of the measured s-s curves.

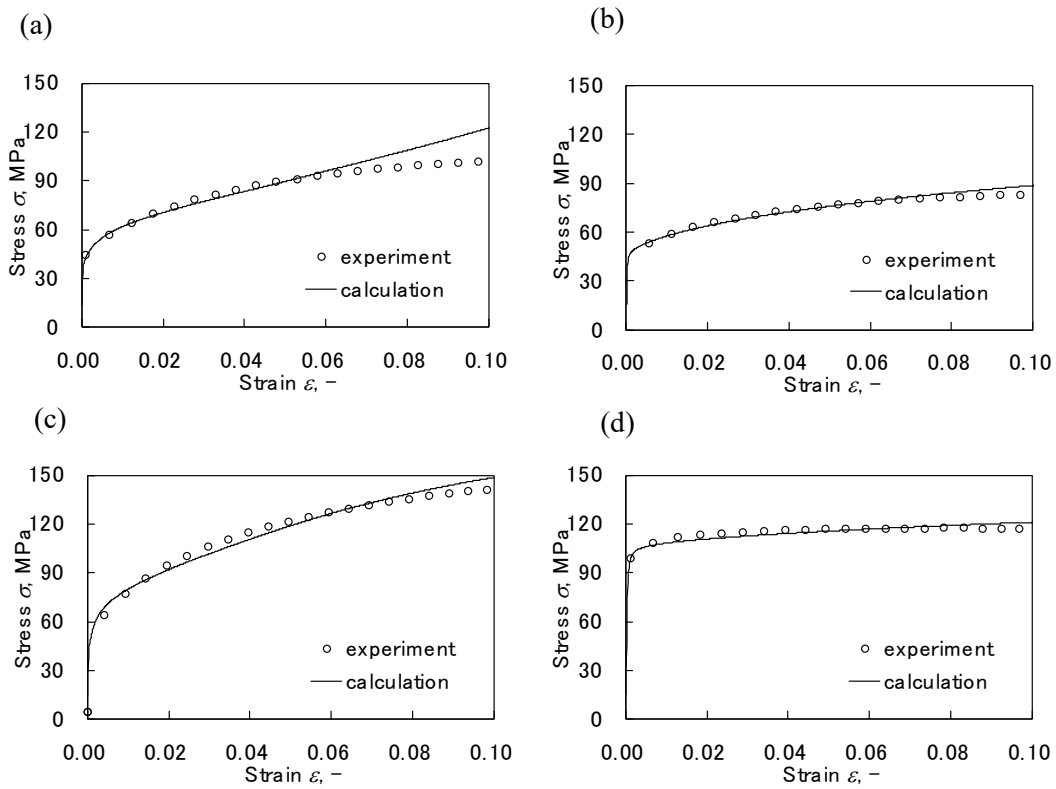

1

Fig. 7 The crystal plasticity parameters appear in Table 2 are fitted with the experimentally obtained s-s curves;
HSS1: austenite phase at 750 °C (a), ferrite/pearlite phase at 750 °C (b),
HSS2 : austenite phase at 720 °C (c), ferrite/pearlite phase at 720 °C (d).

2

Table 2 Crystal plasticity calculation parameters. The relevant temperature is 750 ºC for HSS1 and 720 ºC for HSS2.

	austenite		ferrite/pearlite	
Steel grade	HSS1	HSS2	HSS1	HSS2
Bulk modulus (MPa)	135833	135833	150000	150000
Shear modulus (MPa)	62692	62692	69231	69231
H_0 (MPa)	1400	4000	500	75
τ_0 (MPa)	22	25	27	55
τ_s (MPa)	2300	1800	2000	130
q (-)	1.0	1.0	1.0	1.0
Number of grains	100	100	100	100
C (MPa)	100	100	100	100
d (-)	80	80	80	80

3

Thereby, the crystal plasticity model with the proposed parameter set is one of the solutions that can satisfactory reproduce the constitutive behaviour of HSS1 and HSS2 at given temperature. The back stress parameter set is arbitrarily fixed to $(C, d) = (100, 80)$; this choice will be examined in more depth below.

During phase transformation, randomly distributed seeds start to grow within the austenite grains, with an orientation related to the parent phase by the Kurdjimov-Sachs (K-S) relationship (one of the 24 possible variants is randomly selected). A graphical explanation of the phase transformation calculation is shown in Fig. 8.

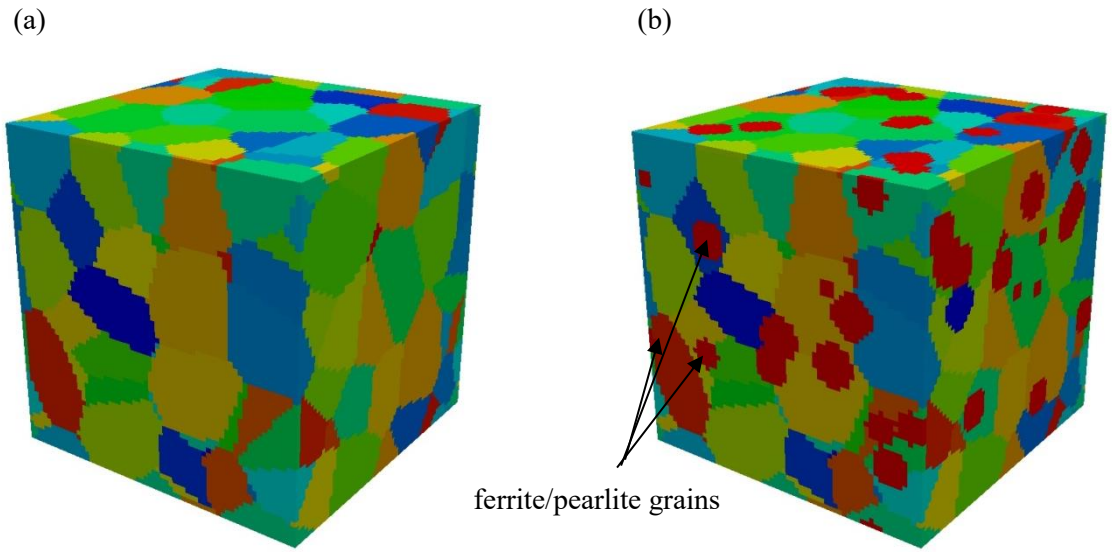

Fig. 8 A graphical explanation of imaginary microstructures at initial state (a) with 100 grains and during phase transformation (b) in the RVE which comprises $64 \times 64 \times 64$ calculation points. The contour represents each grain. The initial microstructure has 100 austenite grains of Voronoi polyhedra; they are $x - y - z$ periodic and have random crystallographic orientations. During phase transformation, 100 new ferrite/pearlite grains nucleate at the random points inside the RVE. The ferrite/pearlite grains, having larger volume than those of austenite, grow isotropically.

As phase transformation progresses, the macroscopic volume expansion (mean value calculated over the RVE) occurs as a consequence of the microscopic (local calculation points) volume expansion. From the exact theoretical result by Leblond [21] for an isotropic polycrystalline aggregate undergoing phase transformation without macroscopic applied stress, the mean strain of the polycrystal reads:

$$\bar{\varepsilon} = \bar{\varepsilon}^m = \beta\xi \tag{17}$$

where $\bar{\varepsilon}$ is the mean strain caused by mean transformation strain $\bar{\varepsilon}^m$, β is the total transformation strain and ξ is the macroscopic volume fraction of daughter (ferrite/pearlite) phase. The β values for HSS1 and HSS2 ferrite/pearlite phase transformation were estimated from the experimental results to be 4.13×10^{-3} and 3.91×10^{-3} respectively. For the case of phase transformation without pre-straining, the predicted macroscopic transformation strain evolution in HSS1 is shown in Fig. 9 (a) without back stress effect and (b) with back stress effect. The same material data as shown in Table 2 (relevant to 750 °C) other than back stress parameters are used. From these results, it is obvious that the transformation strain is isotropic and does not depend on the level of back stress.

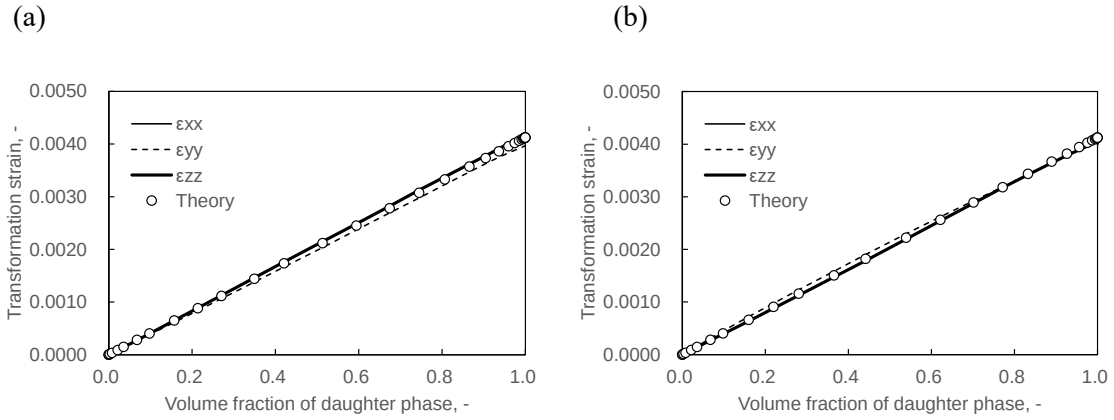

Fig. 9 Comparison of the three strain components predicted with the FFT approach (solid and dashed lines) and the macroscopic one assessed by the Leblond theory (open symbols) without back-stress effect (a) $(C, d) = (0, 0)$ and with back-stress effect (b) $(C, d) = (100, 80)$.

The choice of these back stress parameters (C, d) appear in equation (12) indeed depend on the material. Bandyopadhyay et al. [22] have recently reported the values $(C, d) = (5997, 31)$ for a nickel based super alloy. These values are much larger than those found for a 4340 steel $(C, d) = (100, 30)$ reported by Bennett et al. [23]. Considering the material type, the parameters proposed by Bennett et al. should be quite similar to those that should be retained for our HSS1 and HSS2 steels. In the present case, the parameter d, which quantifies the recovery effect, should be larger than the values proposed in the literature because of the difference in temperature; high temperature problems in the present work and ambient temperature problems in the literature. To consider the influence of the elevated temperature (d should be higher than 30), and the reproductivity of the experimental-based stress/strain curves, the parameters $(C, d) = (100, 80)$ are finally retained for all simulations.

Using these parameters, pre-tension/compression calculations followed by unloading and phase transformation under macroscopic stress-free (zero load) condition have been conducted. A uniaxial tension in z-direction up to 10% macroscopic strain (i.e. averaged on the RVE), is simulated. Note that only 10% pre-deformation calculations are conducted because it was hardly possible to identify the proper parameters for the crystal plasticity calculation up to 30% deformation. The reason behind the discrepancies of s-s curves between calculation and experiment at high strain range is presumably the capability of crystal plasticity constitutive model that this study applies. In this simulation, the six macroscopic strain components are controlled by optimising $\hat{\boldsymbol{\varepsilon}}(\mathbf{0})$ to achieve z-direction uniaxial stress condition with a strain increment in one step equals to $\delta\varepsilon_{zz} = 0.01\%$. Prior to the transformation calculation, the unloading process is simulated with about 2 MPa decrease in σ_{zz} at each step until the stress-free condition is reached. When unloading is completed, phase transformation is set to start as described above.

3.4. Simulation results and discussion

The simulated macroscopic strains in the three directions during phase transformation after pre-tension are shown in Fig. 10 (a-b). Note that the strains at the start of the phase transformation are shifted to zero on the graph to give a better understanding of the transformation behaviour. The resulting transformation strains of HSS1 are now anisotropic $\left(\varepsilon_{xx}^{m}, \varepsilon_{yy}^{m}, \varepsilon_{zz}^{m}\right) = (0.5308\%, 0.5255\%, 0.1818\%)$, but taking the average gives exactly the same value as the isotropic (local) transformation strain value, equals to 0.413%.

As shown in Fig. 10 (a-b), a significant back stress effect on anisotropic transformation strain is observed: the transformation strain in the pre-strained direction (z-direction) shows a smaller value than the other strain components. A similar trend is observed for HSS2, which presents a larger degree of anisotropy. In the same manner as HSS1, the transformation strains of HSS2 are strongly anisotropic $\left(\varepsilon_{xx}^{m}, \varepsilon_{yy}^{m}, \varepsilon_{zz}^{m}\right) = (0.5446\%, 0.5745\%, 0.0551\%)$, but the average of these values is in accordance with the isotropic local transformation strain value estimated at 0.391%. While the qualitative behaviours of pre-deformation effect on the following transformation strains are well in accordance with the experimental ones, anisotropic effects estimated by the simulation for both HSS1 and HSS2 appear to be much stronger than those obtained experimentally. This comparison in HSS1 is summarised in Fig. 10 (c); the anisotropy effect (difference between isotropic and anisotropic strain values) by simulation is 0.231% while by experiment is 0.045%, therefore 5.2 times for HSS1 while 9.6 times for HSS2 more significant effect is estimated by simulation. This discrepancy may be caused by the annihilation of dislocations during the time interval between straining and the onset of phase transformation (HSS2 has longer interval than HSS1), which will in turn reduces the back-stress. This annihilation is not considered in our modelling. These gaps can be narrowed by, for example, stress relaxation tests and an implementation of the dislocation annihilation effect in the numerical model.

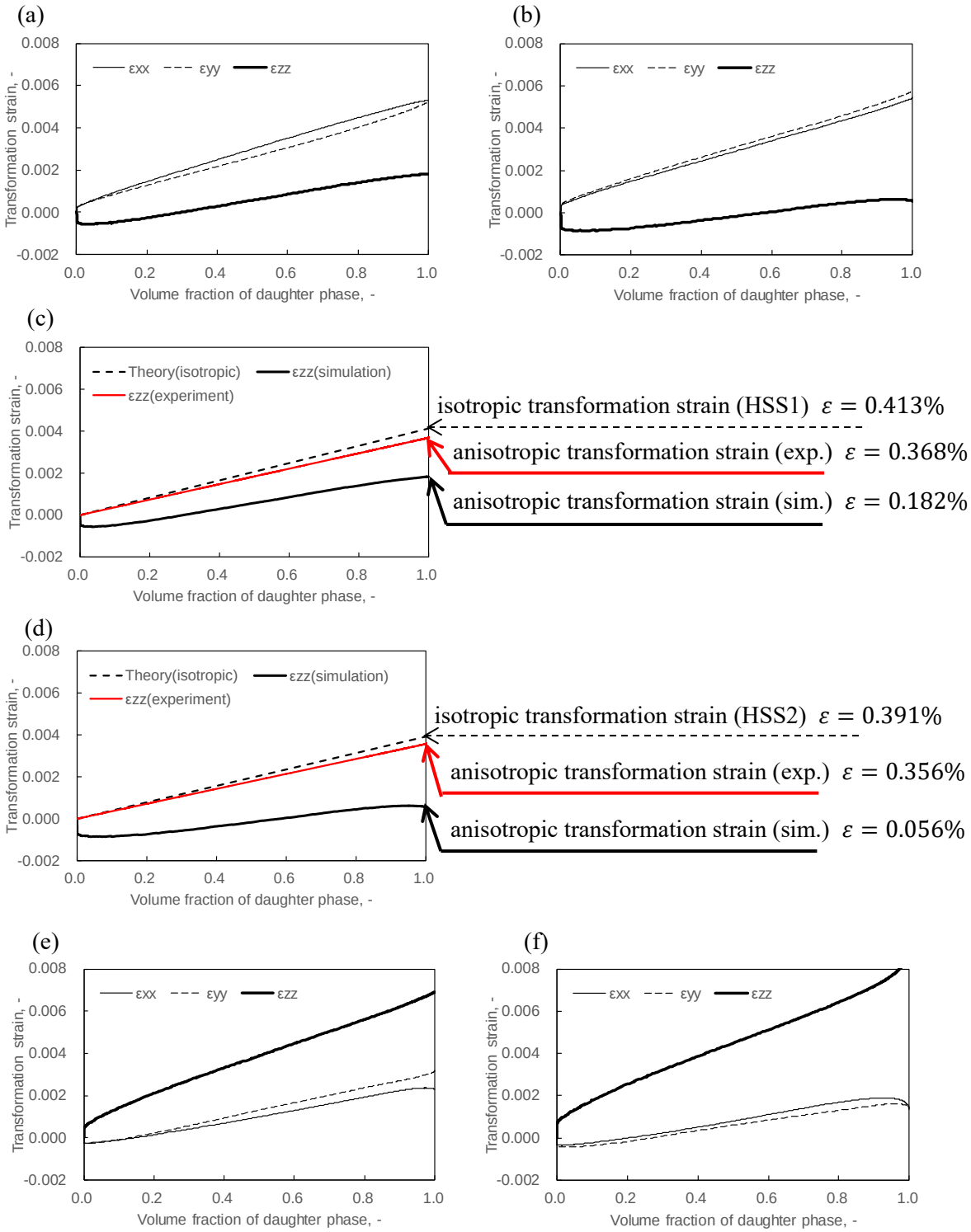
(a)
(b)
(c)
(d)
(e)
(f)
εxx
εyy
εzz
Transformation strain, -
Volume fraction of daughter phase, -
Theory(isotropic)
εzz(simulation)
εzz(experiment)
isotropic transformation strain (HSS1) $\varepsilon = 0.413\%$
anisotropic transformation strain (exp.) $\varepsilon = 0.368\%$
anisotropic transformation strain (sim.) $\varepsilon = 0.182\%$
isotropic transformation strain (HSS2) $\varepsilon = 0.391\%$
anisotropic transformation strain (exp.) $\varepsilon = 0.356\%$
anisotropic transformation strain (sim.) $\varepsilon = 0.056\%$

1

Fig. 10 Predicted evolution of the transformation strains during transformation after 10% pre-straining: pre-tension :
HSS1 (a) and HSS2 (b), comparison of transformation strain between simulation and experiment for HSS1 (c) and for HSS2 (d), pre-compression : HSS1 (e) and HSS2 (f).
Both steel grades have the same qualitative tendency of transformation strain anisotropy, namely the transformation strain in the z direction (tensioned direction) is smaller than those in the other two directions reflecting the directional hardness caused by the pre-straining process. Inversely, the transformation strain in the z direction (compressed direction) is larger than those in the other two directions.

The performed calculations show that, during tension, the back stress develops in the mother (austenite) phase and induces the anisotropy of the subsequent transformation strain. The observed difference in s-s curves between HSS1 and HSS2 may be attributed to the intensity of the anisotropy as HSS2 is slightly harder than HSS1 reflecting the Nb precipitation effect.
In addition, the pre-compression case is to verify the above discussion developed for the case of pre-tension. Again, a pre-compression calculation is conducted down to -10% strain in the z-direction. The rest of the procedure is the same as pre-tension case. The results show the totally opposite behaviour to the ones with pre-tension case, namely, the strain in z-direction during phase transformations appear to be higher than the other direction strain components as shown in Fig. 10 (e-f). The transformation strain is $\left(\varepsilon_{xx}^{m}, \varepsilon_{yy}^{m}, \varepsilon_{zz}^{m}\right) = (0.2278\%, 0.3175\%, 0.6927\%)$ in HSS1 and $\left(\varepsilon_{xx}^{m}, \varepsilon_{yy}^{m}, \varepsilon_{zz}^{m}\right) = (0.1315\%, 0.1372\%, 0.9057\%)$ in HSS2.
In order to investigate the back stress development during the simulation sequence, an average back-stress is calculated on all slip systems as:

$$\bar{a} \equiv \sqrt{\sum_{\alpha} a^{(\alpha)^2}}. \tag{18}$$

Its variation during loading, unloading and phase transformation is shown in Fig. 11 (a) for HSS1 and (b) for HSS2. It is worth noting that the back stress during the unloading process first shows a rapid decrease, reflecting the reversal of the loading direction, but then increases again. This increase in back stress reflects the occurrence of plastic deformation during unloading [24]. From the microscopic point of view, some grains are indeed still in the plastic regime during unloading, resulting also in the marginal decrease in the elastic modulus. Then, in conjunction with the transformation evolution, the average back stress decreases, resulting in anisotropy. By looking at Fig. 10, it is seen that the anisotropy predominantly occurs at the early stage where even a negative transformation strain in z-

direction is observed. Then, as the back stress relaxes, the strain in the z-direction begins to increase as a normal transformation strain.

(a) (b)

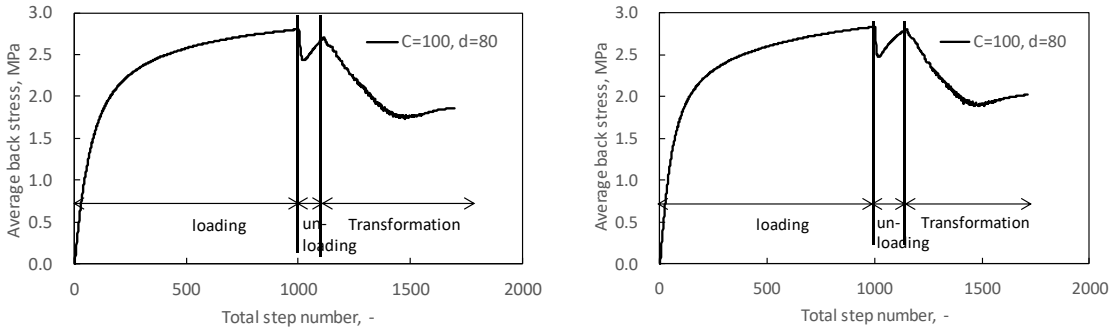

Fig. 11 The predicted evolution of the back stress during the loading-unloading-transformation sequence for HSS1 (a) and HSS2 (b) pre-tension case. The average back stress value decreases with the inverse of straining direction, while it increases again even during unloading. This implies the plastic deformation occurrence during unloading. At the initial stage of phase transformation, plastic strain, which accompanies with the isotropic transformation strain, develops in favour of releasing the accumulated back stress during pre-tension.

This confirms the above explanation that the pre-straining makes an effect on the anisotropic transformation strain even though the local transformation strain is isotropic. Therefore, the back stress induced anisotropy is an origin of plastic (i.e. necessarily anisotropic) deformation during phase transformation sharing the similar mechanistic nature with heterogeneous microstructure [64-69] and applied external stress induced transformation plasticity [70-74].

4. Conclusion

In this paper, the influence of a pre-deformation on the subsequent ferrite/pearlite transformation features in two high strength steels (with/without Nb) at high temperature, has been studied both experimentally and numerically. It has thus been revealed that:

- Pre-straining results in an anisotropic transformation strain. The more severe pre-straining the more significant anisotropy occurs.
- The anisotropy is less significant with Nb content.
- Pre-tension decreases the same directional transformation strain, whereas pre-compression

increases the same directional transformation strain.

- Even though anisotropic, total transformation strain value remains the same as that of the isotropic case.

To interpret these phenomena, some simulations have been performed using a crystal plasticity constitutive law and the Armstrong-Frederick hardening law, yielding:

- The behaviour of anisotropic transformation strain found in the experiments can be explained qualitatively by the back-stress induced by pre-straining.
- The anisotropy effect found by the simulation is more significant than that by experiment because of the dislocation annihilation during the interval between pre-straining and the onset of phase transformation at high temperature.

This result may have important consequences for some industrial processes such as hot rolling, for which there is still a need to better control the final dimensions (mainly the width) of the rolled sheets. The proposed methodology will thus be applied in the future to real industrial schedules.

Funding

No funding was received to assist with the operation of this research.

Conflicts of interest

There are no conflicts of interest.

Data availability statement

This article has no associated data generated or analysed.

Author contribution statement

Conceptualisation, T. Otsuka, R. Brenner and B. Bacroix ; Formulation, T. Otsuka, R. Brenner and B. Bacroix, Programming, T. Otsuka and R. Brenner, Conduct simulations, T. Otsuka; Validation, T. Otsuka, R. Brenner and B. Bacroix; Original Draft Preparation, T. Otsuka; Writing – Review & Editing, T. Otsuka, R. Brenner and B. Bacroix; Supervision, R. Brenner and B. Bacroix

References

[1] L. Taleb , S. Petit-Grostabussiat, Elastoplasticity and phase transformations in ferrous alloys: Some discrepancies between experiments and modeling, J. Phys. IV France, 12, 11, 187-194 (2002)

[2] L. Taleb , S. Petit, New investigations on transformation induced plasticity and its interaction with classical plasticity, Int. J. Plasticity, **22**, 1, 110-130 (2006)

[3] K. Oshita, S. Nagaki, S. Itakura , S. Nomoto, Evaluation of bending transformation plasticity of S45C subjected to pre-plastic deformation, J. Soc. Mater. Sci., Japan, **68**, 6, 485-490 (in Japanese) (2019)

[4] H. Li, M. Xu , Z.-T. Li, Transformation behavior and acceleration of low-temperature bainite in high carbon chrominum steel, Materials Research Express, **5**, 7, 076520 (2018)

[5] D. S. Schicchi , M. Hunkel, Effect of Pre-strain and High Stresses on the Bainitic Transformation of Manganese-boron Steel 22MnB5, Metallurgical and Materials Transactions A, **49**, 2011-2025 (2018)

[6] P. Drillet, Study of cracks propagation inside the steel on press hardened steel zinc based coatings, 8th Int. Conf. GALVATECH 2011, Genova, 21-25 (2011)

[7] P. Drillet, R. Grigorieva, G. Leuillier , T. Vietoris, Study of cracks propagation inside the steel on press hardened steel zinc based coatings, La Metallurgia Italiana, **1**, 3-8 (2012)

[8] R. Colás, L. Leduc , M. Neri, Prediction of shape defects during cooling of hot rolled low carbon steel strip, Ironmaking & Steelmaking, **31**, 1, 93-96 (2004)

[9] X. Wang, F. Li, Q. Yang , A. He, FEM analysis for residual stress prediction in hot rolled steel strip during the run-out table cooling, Appl. Math. Modell., **37**, 1-2, 586-609 (2013)

[10] J. Ilmola, A. Pohjonen, S. Koskenniska, O. Seppälä, O. Leinonen, J. Jokisaari, J. Pyykkönen , J. Larkiola, Coupled heat transfer and phase transformations of dual-phase steel in coil cooling, Mater. Commun., **26**, 101973 (2021)

[11] H. Wu, J. Sun, X. Lu, W. Peng, Q. Wang , D. Zhang, Predicting stress and flatness in hot-rolled strips during run-out table cooling, J. Manuf. Process., **84**, 815-831 (2022)

[12] H. Wu, J. Sun, W. Peng , D. Zhang, Analytical model of hot-rolled strip residual stress and flatness in run-out table cooling, Appl. Math. Modell., **120**, 175-198 (2023)

[13] X. J. Jin, N. Min, K. Y. Zheng , T. Y. Hsu (Xu Zuyao), The effect of austenite deformation on bainite formation in an alloyed eutectoid steel, Materials Science and Engineering A **438-440**, 170-172 (2006)

[14] X. H. Hu, X. Sun, L. G. Hector Jr. , Y. Ren, Individual phase constitutive properties of a TRIP-assisted QP980 steel from a combined synchrotron X-ray diffraction and crystal plasticity approach, Acta Mater., **132**, 15, 230-244 (2017)

[15] W. Wu, Y.-W. Wang, P. Makrygiannis, F. Zhu, G. A. Thomas, L. G. Hector Jr., X. Hu, X. Sun , Y. Ren, Deformation mode and strain path dependence of martensite phase transformation in a medium manganese TRIP steel, Mater. Sci. Eng. A, **711**, 10, 611-623 (2018)

[16] F. Abu-Farha, X. Hu, X. Sun, Y. Ren, L. G. Hector Jr., G. Thomas , T. W. Brown, In situ local measurement of austenite mechanical stability and transformation behavior in third-generation

advanced high-strength steels, Metall. Mater. Trans. A, **49**, 2583-2596 (2018)

[17] T. Otsuka, R. Brenner , B. Bacroix, FFT-based modelling of transformation plasticity in polycrystalline materials during diffusive phase transformation, Int. J. Eng. Sci., **127**, 92-113 (2018)

[18] T. Otsuka, D. Satani, K. Yamamoto, K. Okamura, R. Brenner , B. Bacroix, Microstructure and heat treatment effect on transformation strain in steels: part 2 modelling, Mater. Sci. Technol., **35**, 2, 187-194 (2019)

[19] T. Otsuka, B. Bacroix , R. Brenner, Back stress effect on anisotropic dilatation during phase transformation of steels, TMP 2016 - 5th International Conference on ThermoMechanical Processing, Milan (2016)

[20] C. O. Frederick , P. J. Armstrong, A mathematical representation of the multiaxial Bauschinger effect, Mater. High Temp., **24**, 1, 1-26 (2007)

[21] A. Eghtesad , M. Knezvic, High-performance full-field crystal plasticity with dislocation-based hardening and slip system back-stress laws: Application to modeling deformation of dual-phase steels, J. Mech. Phys. Solids, **134**, 103750 (2020)

[22] T. Zirkle, T. Zhu , D. L. McDowell, Micromechanical crystal plasiticity back stress evolution within FCC dislocation substructure, Int. J. Plast., **146**, 103082 (2021)

[23] X. Long, K. Chong, Y. Su, C. Chang , L. Zhao, Meso-scale low-cycle fatigue damage of polycrystalline nickel-based alloy by crystal plasticity finite element method, Int. J. Fatigue, **175**, 107778 (2023)

[24] T. Park, L. G. Hector Jr., X. Hu, F. A.-Farha, M. Fellinger, H. Kim, R. Esmaeilpour , F. Pourboghrat, Crystal plasticity model of third generation multi-phase AHSS with martensitic transformation, Int. J. Plasticity, **120**, 1-46 (2019)

[25] D. Connolly, C. Kohar, W. Muhammad, L. Hector Jr., R. Mishra , K. Inal, A coupled thermomechanicalc crystal plasticity model applied to Quenched and Partitioned steel, Int. J. Plasticity, **133**, 102757 (2020)

[26] F. Barbe, R. Quey , L. Taleb, Numerical modelling of the plasticity induced during diffusive transformation. Case of a cubic array of nuclei, Eur. J. Mech. -A/Solids, **26**, 4, 611-625 (2007)

[27] F. Barbe, R. Quey, L. Taleb , E. Souza de Cursi, Numerical modelling of the plasticity induced during diffusive transformation. An ensemble averaging approach for the case of random arrays of nuclei, Eur. J. Mech. A/Solids, **27**, 1121-1139 (2008)

[28] F. Barbe , R. Quey, A numerical modelling of 3D polycrystal-to-polycrystal diffusive phase transformations involving crystal plasticity, Int. J. Plast., **27**, 6, 823-840 (2011)

[29] Y. El Majaty, R. Brenner , J.-B. Leblond, FFT-based micromechanical simulations of

transformation plasticity. Comparison with a limit-analysis-based theory, Eur. J. Mech. - A/Solids, **86**, 104152 (2021)

[30] A. Tahimi, F. Barbe, L. Taleb , S. Meftah, Experiment-based analyses of martensitic transformation plasticity predictions from different models in cases of pre-hardening and gradually varying loads, Compt. Mater. Sci., **64**, 25-29 (2012)

[31] R. A. Lebensohn, R. Brenner, O. Castelnau , A. D. Rollett, Orientation image-based micromechanical modelling of subgrain texture evolution in polycrystalline copper, Acta Materialia, **56**, 3914-3926 (2008)

[32] A. Belkhabbaz, B. Bacroix , R. Brenner, Investigation of the elastoplastic behavior of fcc polycrystals using a FFT numerical scheme, Revue roumaine des sciences techniques, Série de mécanique appliquée, **60**, 5-23 (2015)

[33] B. Liu, D. Raabe, F. Roters, P. Eisenlohr , R. Lebensohn, Comparison of finite element and fast Fourier transform crystal plasticity solvers for texture prediction, Modell. Simul. Mater. Sci. Eng., **18**, 085005 (2010)

[34] P. Siegmann, L. Felipe-Sesé , F. A. Díaz, An alternative approach for improving DIC by using out-of-plane displacement information, Opt. Laser Eng., **128**, 105996 (2020)

[35] M. Badaloni, P. Lava, M. Rossi, G. Chiappini , D. Debruyne, Out-of-plane motion evaluation and correction in 2D DIC, Adv. Opt. Methods in Exp. Mech., **3**, 181-187 (2016)

[36] M. Bertin, C. Du, J.-P. Hoefnagels , F. Hild, Crystal plasticity parameter identification with 3D measurements and Integrated Digital Image Correlation, Acta Mater., **116**, 1, 321-331 (2016)

[37] R. Kaczmarek, J.-C. Dupré, P. Doumalin, O. Pop, L. Teixeira , M. Huger, High-temperature digital image correlation techniques for full-field strain and crack length measurement on ceramics at 1200°C: Optimization of speckle pattern and uncertainty assessment, Optics and Lasers in Eng., **146**, 106716 (2021)

[38] T. Otsuka, M. Sakamoto, Y. Takamachi, Y. Higashida, Y. Segawa , S. Takeshima, An online rolling model for plate mill using parallel computation, ISIJ int., **57**, 11, 2042-2048, (2017)

[39] H. Moulinec , P. Suquet, A numerical method for computing the overall response of nonlinear composites with complex microstructure, Comput. Method. Appl. M., **157**, 68-94 (1998)

[40] A. Belkhabbaz, R. Brenner, N. Rupin, B. Bacroix , J. Fonseca, Prediction of the overall behavior of a 3D microstructure of austenitic steel by using FFT numerical scheme, Procedia Eng., **10**, 1883-1888 (2011)

[41] R. A. Lebensohn, R. Brenner, O. Castelnau , A. D. Rollett, Orientation image-based micromechanical modellilng of subgrain texture evolution in polycrystalline copper, Acta Mater., **56**, 3914-3926 (2008)

[42] S.-B. Lee, R. Lebensohn , A. Rollett, Modeling the viscoplastic micromechanical response of two-phase materials using Fast Fourier Transforms, Int. J. Plasticity, **27**, 707-727 (2011)

[43] R. Lebensohn, A. Kanjarla , P. Eisenlohr, An elasto-viscoplastic formulation based on fast Fourier transforms for the prediction of micromechanical fields in polycrystalline materials, Int. J. Plasticity, **32-33**, 59-69 (2012)

[44] L. Li, L. Shen , G. Proust, A texture-based representative volume element crystal plasticity model for predicting Bauschinger effect during cyclic loading, Mater. Sci. Eng. A, **608**, 174-183 (2014)

[45] R. Bandyopadhyay, S. E. Gustafson, K. Kapoor, D. Naragani, D. C. Pagan , M. D. Sangid, Comparative assessment of back stress models using high-energy X-ray diffraction microscopy experiments and crystal plasticity finite element simulations, Int. J. Plasticity, **136**, 102887 (2021)

[46] D. Zhou, X. Wang, R. Wang, T. Zhang, X. Yang, Y. Jiang, X. Zhang, J. Gong , S. Tu, An extended crystal plasticity model to simulate the deformation behaviors of hybrid stress–strain controlled creep-fatigue interaction loading, Int. J. Fatigue, **156**, 106680 (2022)

[47] D. Agius, K. Kourousis , C. Wallbrink, A modification of the multicomponent Armstrong–Frederick model with multiplier for the enhanced simulation of aerospace aluminium elastoplasticity, Int. J. Mech. Sci., **144**, 118-133 (2018)

[48] X. Ren, S. Yang, W. Zhao , G. Wen, A crystal plasticity-based constitutive model for ratchetting of cyclic hardening polycrystalline metals, Int. J. Dyn. Control, **8**, 1161-1168 (2020)

[49] R. J. Asaro, Micromechanics of crystals and polycrystals, Adv. Appl. Mech., **23**, 1-115 (1983)

[50] R. J. Asaro, Crystal Plasticity, ASME J. Appl. Mech., **50**, 921-934 (1983)

[51] R. J. Asaro , A. Needleman, Texture development and strain hardening in rate dependent polycrystals, Acta Metall., **33**, 923-953 (1985)

[52] J. W. Hutchinson, "Elastic-plastic behaviour of poly crystalline metals and composites," Proc. of Roy. Soc., A.319, pp. 247-272, 1970.

[53] D. Peirce, R. J. Asaro , A. Needleman, An analysis of non-uniform and localized deformation in ductile single crystals, Acta Metall., **30**, 1087–1119 (1982)

[54] L. Zhang, L. Zhao, R. Jiang , C. Bullough, Crystal plasticity finite-element modelling of cyclic deformation and crack initiation in a nickel-based single-crystal superalloy under low-cycle fatigue, Fatigue Fract. Eng. Mater. Struct., **43**, 8, 1769-1783 (2020)

[55] P. Cetlin, E. Corrêa , M. Aguilar, The effect of the strain path on the work hardening of austenitic and ferritic stainless steels in axisymmetric drawing, Metall. Mater. Trans. A, **34A**, 589-601 (2003)

[56] M. Moshtaghi , S. Sato, Characterization of Dislocation Evolution in Cyclically Loaded Austenitic and Ferritic Stainless Steels via XRD Line-profile Analysis, ISIJ int., **59**, 9, 1591-1598 (2019)

[57] Y. Imai , Y. Shono, The effects of grain size and precipitate on strength of Nb-treated steels, Trans. ISIJ, **9**, 335-342 (1969)

[58] N. Nakada, M. Fujihara, T. Tsuchiyama , S. Takaki, Effect of phosphorus on Hall-Petch coefficient in ferritic steel, ISIJ int., **51**, 7, 1149-1173 (2011)

[59] R. Armstrong, Crystal Engineering for Mechanical Strength at Nano-Scale Dimensions, Crystals, **7**, 10 (2017)

[60] Y. Wang, J. Kang, Y. Peng, T. Wang, N. Hansen , X. Huang, Hall-Petch strengthening in Fe-34.5Mn-0.04C steel cold-rolled, partially recrystallized and fully recrystallized, Scripta Mater., **155**, 41-45 (2018)

[61] J. B. Leblond, G. Mottet , D. C. Devaux, A Theoretical and Numerical Approach to the Plastic Behaviour of Steels During Phase Transformations-I. Derivation of General Relations, J. Mech. Phys. Solids, **34**, 4, 395-409 (1986)

[62] V. Bennett , D. McDowell, Polycrystal orientation distribution effects on microslip in high cycle fatigue, Int. J. Fatigue, **25**, 27-39 (2003)

[63] M. O. Andar, T. Kuwabara, S. Yonemura , A. Uenishi, Elastic-plastic and inelastic characteristics of high strength steel sheets under biaxial loading and unloading, ISIJ int., **50**, 4, 613-619 (2010)

[64] T. Kop, J. Sietsma , S. van der Zwaag, Anisotropic dilatation behaviour during transformation of hot rolled steels showing banded structure, Mater. Sci. Technol., **17**, 12, 1549-1574 (2001)

[65] R. Jaramillo, M. Lusk , M. Mataya, Dimensional anisotropy during phase transformations in a chemically banded 5140 stee. Part I: experimental investigation, Acta Mater., **52**, 851-858 (2004)

[66] R. Jaramillo , M. Lusk, Dimensional anisotropy during phase transformations in a chemically banded 5140 stee. Part II: modelling, Acta Mater., **52**, 859-867 (2004)

[67] T. Siwecki, T. Koziel, B. Hutchinson , P. Hansson, Effect of Micro-Segregation on Phase Transformation and Residual Stress, Mater. Sci. Forum Vols. **539-543**, 4596-4601 (2007)

[68] B. Hutchinson, Critical assessment 16: Anisotropy in metals, Mater. Sci. Technol., **31**, 1393-1401 (2015)

[69] T. Otsuka, D. Satani, K. Yamamoto, K. Okamura, R. Brenner , B. Bacroix, Microstructure and heat treatment effect on transformation strain in steels: part1 experiment, Mater. Sci. Technol., **35**, 2, 181-186 (2019)

[70] G. W. Greenwood , R. Johnson, The deformation of metals under small stresses during phase

transformations, Proc. Roy. Soc. London, **A283**, 1394, 403-422 (1965)

[71] J. B. Leblond, J. Devaux , J. C. Devaux, Mathematical modelling of transformation plasticity in steels I: Case of ideal-plastic phases, Int. J. Plasticity, **5**, 6, 551-572 (1989)

[72] J. Leblond, Matahematical modelling of transformation plasticity in steels II: Coupling with strain hardening phenomena, Int. J. Plasticity, **5**, 6, pp. 573-591 (1989)

[73] T. Inoue, Transformation Plasticity, J. Soc. Mater. Sci., Japan, **64**, 4, 247-257 (in Japanese) (2015)

[74] T. Otsuka , N. Legrand, Effect of Cooling Rate on Transformation Plasticity of 0.45% Carbon Steel, ISIJ international, **60**, 4, 721-730 (2020)

1